Journal of Harbin Engineering University
ISSN: 1006-7043
Vol X No. Y
Month 2024

Prediction and Reduction of Pressure Loss in a Duct with 90^0 Sharp Bend

L.Uyega[1], N. Subaschandar*
Department of Mathematics and Statistical Sciences, Botswana International University of Science and Technology, Private Bag 16, Palapye, Botswana.
[1]Undergraduate student

Abstract- Bent pipes and ducts are used extensively in industrial complexes mainly due to space constraints. However, bends and pipes cause pressure loss and generate flow separation inside the pipes and ducts reducing the efficiency of fluid transport. In this report a duct of sharp 90^0 is taken into consideration to predict static pressure loss in it. It is then changed into other configurations to predict if the change from sharp corners to smooth curved corners can reduce the static pressure loss coefficient. EasyCFD software was used to predict the pressure loss for four configurations. The SST turbulence model has been used to carry out the computations. The square duct with both sharp corner incurred maximum static pressure loss coefficient of 1.467 whereas making both corners curved reduced the static pressure loss coefficient to 0.212, a reduction of about 85%. It is shown that major portion of the static pressure loss can be recovered (about 82 %) by giving a smooth curvature to the inner corner alone.

Keywords-- Turbulence model, Pressure loss, 90^0 bend, square duct, curved bend

1. Introduction

A 90^0 bent sharp elbow is ordinarily used in numerous piping and ducting systems to join different components. It is usual that the air-conditioning and ventilation ducting systems and the mill-duct transporting systems contain not only curved 90° elbow bends with various curvature ratios, but also right-angled sharp 90° elbow bends due to space limitations. Curved elbows cause less energy losses than sharp elbows; however, their production is more costly. It is well established that during the fluid flow motion inside a pipe with sharp elbow, a recirculatory secondary motion of the fluid flow is established, and it is overlaid on its principal streamwise flow. The secondary recirculatory flow is produced due to a discrepancy between centrifugal force and pressure gradient close to the bend of the pipe wall in the radial direction of the bend curvature. In general, the structure of the recirculatory flow is dependent on the radius of the bend curvature and Reynolds number of the fluid flow. If the radius of curvature of the bend is larger than 1.5 (i.e., $R_c/D>1.5$), the secondary fluid flow containing a pair of counterrotating vortices are produced. Also, the mean velocity distribution of the principal streamwise component fluid flow is changed and moved away from the centre of the curvature of the bend. If R_c/D is less than 1.5, the

fluid flow develops into an unsteady flow due to fluid flow separation happening instantly downstream of the bend [1,2]. The fluid flow in the downstream zone of a 90^0 turn is very significant for the principal and secondary cooling systems of nuclear power plants, in which numerous bends are used to join the elements. The deformation in the streamwise mean velocity distribution of the coolant by a bend can impact the distribution of heat transfer characteristics. When the curvature radius of a bend is small enough to generate a fluctuating fluid flow after the sharp elbow, the downstream duct can experience fluctuating mechanical stress, which may cause structural weakness in the ducting system[3]. In the past, many researchers have studied turbulent flows in pipes with elbows by means of theoretical, experimental, and computational methods. Weske [1] studied the mean velocity profile at the exit of elbows having different shapes of cross-sections including round, elliptical, square, and rectangular cross sections at Reynolds numbers in the range of 0.2×10^6 to 0.6×10^6 for the design of an aircraft duct. Sudo et al. [4] carried out experiments for turbulent fluid flow in a 90^0 bent pipe with $R_c/D=2$. The study

used a hot-wire anemometer to measure streamwise velocity and circumferential velocity for a turbulent fluid flow with Reynolds number of 60,000. Al-Rafai et al. [5] performed research of a turbulent fluid flow inside circular pipe bends to study the impact of radius of curvature of the bend on the fluid flow. Two bends with radii of curvature for the bend of 3.49 and 6.975 were operated, and the flow Reynolds number was about 34,000. Homicz[6] carried out computational simulations of the fluid flow through a 90^0 elbow with a non-dimensional radius of curvature of 1.4 and at a flow Reynolds number of 5.4×10^5 to justify the Flow-Accelerated Corrosion (FAC) experiment conducted by Korea Atomic Energy Research Institute (KAERI). In a later study, Tanaka et al. [7] employed a large eddy simulation (LES) method using a standard Smagorinsky model with an associated wall function rule for fluid flows inside elbows with different radii of curvature at various Reynolds number situations. Many of the above-mentioned investigations focused only on the fluid flow structure in the close neighbourhood of the elbow and only a limited number of studies were carried out in the flow in the downstream zone of the elbows [4,5,8-11]. The knowledge of the fluid flow structure in the downstream zone of the elbow is important to understand the dissipation characteristics of the secondary fluid flow and to correctly assess the growth of the fluid flow structure. Additionally, a knowledge of the dissipation characteristics is important in evaluating the distance needed for the elbow effects to be dissipated and in modelling the effects connected with fluid flow restrictions.

When a flow takes place under the influence of pressure in a horizontal duct, the flow experiences a decrease in pressure in the streamwise direction because of the net energy flux into any section of the pipe is adjusted by a loss of energy due to viscous dissipation. In the fully developed duct flow, the fluid sticks to the wall and increases to a maximum at the middle of the straight duct. If the flow is turbulent, the loss of energy is large mainly because of turbulent mixing of the fluid and the velocity profile is flatter near the centre of the duct. When bend ducts are used for various reasons, a penalty in the form of pressure loss is experienced. This excessive pressure drop in many situations results in increase in fan power, flow reduction and noise. The accurate calculation of pressure losses due to all pipe fittings is important in the proper design, choice of fans and for energy efficient systems[12]. A better performing system would result in significant savings in the initial investment, the operational cost and in the maintenance of the systems. Heating, Ventilation and Air Conditioning (HVAC) engineers and designers look to reduce pressure loss.

In this paper, the effects of corner modifications on the static pressure loss in square duct with a 90^o sharp bend is studied numerically. Inner sharp corner and outer sharp corner have been modified individually to study their effect on the static pressure loss and, also, their combined effect on the static pressure loss. Modified sharp corners were studied at a radius of curvature of $R_c/D=1.33$. Static pressure loss in the duct was the focus of research in this study.

2. Computational Geometry Description

In this section the basic details of geometries studied are presented. The computational geometry, a two-dimensional rectangular elbow of 150mm width and consisting of a horizontal portion of 3.5m long, a sharp 90^0 elbow, and a vertical duct of 1.8m long, is shown in Fig.1. The air is admitted through the inlet of the duct at a uniform speed. The air flow throughout the duct is turbulent and fully developed at the exit. The standard Shear Stress Turbulence model(SST model) has been used in the current study. Computations have been carried out from the point of calculating static pressure loss in the flow at the exit plane. In this study the flow is assumed to be steady, fully turbulent, incompressible with constant viscosity and constant density. Table 1 presents the duct configurations studied and the nomenclature used for those configurations in this paper.

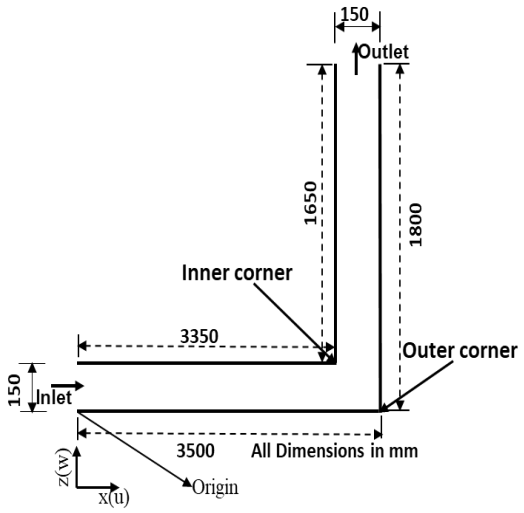

Fig.1 2-D computational domain

TABLE 1. Nomenclature for the configurations

Configurations	Nomenclature
Inner Sharp Outer Sharp	ISOS
Inner Sharp Outer Curved	ISOC
Inner Curved Outer Sharp	ICOS
Inner Curved Outer Curved	ICOC

3. Mathematical Modelling

For describing the governing transport equations, the *x* and *z* coordinates of the Cartesian coordinate system will be used as the independent variables [Fig.1].

3.1. The Navier-Stokes Equations

The turbulent flow studied in this research is governed by the Navier-Stokes equations, which, for a two-dimensional flow situation, may be stated as follows[13-20]:

Horizontal component:

$$\frac{\partial}{\partial x}(\rho u^2)+\frac{\partial}{\partial z}(\rho uw)=\frac{\partial}{\partial x}\left(\Gamma\frac{\partial u}{\partial x}\right)+\frac{\partial}{\partial z}\left(\Gamma\frac{\partial u}{\partial z}\right)-\frac{\partial p}{\partial x}+\frac{\partial}{\partial x}\left(\Gamma\frac{\partial u}{\partial z}\right)+\frac{\partial}{\partial z}\left(\Gamma\frac{\partial u}{\partial x}\right)-\frac{2}{3}\frac{\partial}{\partial x}\left(\mathrm{div}\vec{V}\right) \quad (1)$$

Vertical Component:

$$\frac{\partial}{\partial x}(\rho uw)+\frac{\partial}{\partial z}(\rho w^2)=\frac{\partial}{\partial x}\left(\Gamma\frac{\partial w}{\partial x}\right)+\frac{\partial}{\partial z}\left(\Gamma\frac{\partial w}{\partial z}\right)-\frac{\partial p}{\partial z}+\frac{\partial}{\partial x}\left(\Gamma\frac{\partial w}{\partial z}\right)+\frac{\partial}{\partial z}\left(\Gamma\frac{\partial w}{\partial x}\right)-\frac{2}{3}\frac{\partial}{\partial z}\left(\mathrm{div}\vec{V}\right) \quad (2)$$

In the previous equations, *p* [N/m2] represents pressure. The diffusion coefficient is given by:

$$\Gamma=\mu+\mu_\tau. \quad (3)$$

where μ [Ns/m^2] is the dynamics viscosity and μ_τ is the turbulent eddy viscosity.

Continuity Equation :

The conservation of mass law, or continuity equation, may be stated as :

$$\frac{\partial}{\partial x}(\rho u)+\frac{\partial}{\partial z}(\rho w)=0 \quad (4)$$

3.2. Turbulence Modelling

The properties of a turbulent fluid flow (velocity, pressure, etc.) are not constant in time. Instead, they present fluctuations about an average value. The numerical calculation of the instantaneous value is not amenable with currently available methods and resources, due to the high temporal and spatial frequencies that characterize these flows and, hence the average values only are calculated. EasyCFD[16] implements two turbulence models, namely k-ε and Shear Stress Transport(SST) turbulence models. However, only Shear Stress Transport(SST) turbulence model has been used here in this study. The Shear Stress Transport(SST) turbulence model is described below. The above set of governing transport equations are solved, using suitable boundary conditions for the computational domain, using numerical methods.

The Shear Stress Transport (SST) Turbulence Model: The SST turbulence model is a combination of two widely-used turbulence models, namely, the k-ε and the k-ω turbulence models [21]. According to the study[22], the k-ω turbulence model performs better near the wall but displays a high sensitivity to the ω values in the free stream region, where the k-ε turbulence model displays a better behaviour. The SST turbulence model, thus, represents a blend of these two turbulence models, through a weighting factor calculated based on the nearest surface distance. The governing transport equations are:

$$\frac{\partial}{\partial x}(\rho uk)+\frac{\partial}{\partial z}(\rho wk)=\frac{\partial}{\partial x}\left[(\mu+\sigma_k\mu_t)\frac{\partial k}{\partial x}\right]+\frac{\partial}{\partial z}[(\mu+\sigma_k\mu_t)\frac{\partial k}{\partial z}]+\overline{P_k}-\beta^*\rho\omega k \quad (5)$$

$$\frac{\partial}{\partial x}(\rho u\omega)+\frac{\partial}{\partial z}(\rho w\omega) = \frac{\partial}{\partial x}\left[(\mu+\sigma_\omega\mu_t)\frac{\partial\omega}{\partial x}\right]+\frac{\partial}{\partial z}[(\mu+\sigma_\omega\mu_t)\frac{\partial\omega}{\partial z}]+\frac{\overline{P_k}}{\nu_t}\alpha-\beta^*\rho\omega^2+2(1-F_l)\frac{\rho\sigma_{\omega2}}{\omega}\left(\frac{\partial k}{\partial x}\frac{\partial\omega}{\partial x}+\frac{\partial k}{\partial z}\frac{\partial\omega}{\partial z}\right)$$

(6)

where ω is the frequency of dissipation rate of turbulent kinetic energy[s^{-1}].

The production of turbulent kinetic energy is restricted to stop the build-up of turbulence in flow in stagnant zones:

$$\overline{P_k} = \min(P_k, 10\beta^*\rho k\omega) \quad (7)$$

The weighting function F_l is given by:

$$F_l = \tanh\left\{\left\{\min\left[\max\left(\frac{\sqrt{k}}{\beta^*\omega z},\frac{500\nu}{z^2\omega}\right),\frac{4\rho\sigma_{\omega2}k}{C_{k\omega}z^2}\right]\right\}^4\right\}$$

(8)

and

$$C_{k\omega} = \max\left[2\rho\sigma_{\omega2}\frac{1}{\omega}\left(\frac{\partial k}{\partial x}\frac{\partial\omega}{\partial x}+\frac{\partial k}{\partial z}\frac{\partial\omega}{\partial z}\right),10^{-10}\right]$$

(9)

where z represents the distance to the nearest wall and ν is the laminar dynamic viscosity. F_l is zero away from the rigid surface (k-ε turbulence model) and changes to unit value inside the boundary layer (k-ω turbulence model). With a smooth transition based on z.

The turbulent eddy viscosity is calculated as :

$$\nu_t = \frac{a_1 k}{\max(a_1\omega, SF_2)} \quad (10)$$

where S is the invariant amount of the strain rate, given by:

$$S = \sqrt{S_{ij}S_{ij}} \;;\; S_{ij} = \frac{1}{2}\left(\frac{\partial u_i}{\partial x_j}+\frac{\partial u_j}{\partial x_i}\right) \quad (11)$$

and

$$F_2 = \tanh\left\{\left[\max\left(\frac{2\sqrt{k}}{\beta^*\omega z},\frac{500\nu}{z^2\omega}\right)\right]^2\right\}$$

(12)

The constants are calculated as a blend of the k-ε and the k-ω turbulence models, through the general equation given below:

$$\alpha = F_1\alpha_1+(1-F_1)\alpha_2 \quad (13)$$

The model constants are:

α_1=5/9, β_1=3/40, σ_{k1}=0.85, $\sigma_{\omega1}$=0.5, α_2=0.44, β_2=0.0828, σ_{k2}=1.0, $\sigma_{\omega2}$=0.856, β^*=0.09

The above set of governing equations have been solved, along with appropriate boundary conditions for the computational domain, using numerical methods. Near wall treatment of momentum and turbulence equations as implemented in EasyCFD[16] obeys the suggestions explained in [23]. The simple notion behind the automatic wall functions is to change from a low-Reynolds number scheme to a wall function built on the mesh nodes nearness to the surface. The first order upwind method was used to discretize the momentum equations, turbulent kinetic energy and turbulence dissipation rate equations. The Semi-Implicit Method for Pressure-Linked Equations-Consistent (SIMPLEC) method was implemented for the pressure velocity interactions [16,24].

At the inlet of the computational domain, a uniform velocity condition is given. The exit was considered as a conservative outlet where the streamwise and normal gradients are zero for all parameters. On the walls the zero mean velocity condition was imposed. The computational fluid dynamics software EasyCFD[16] was chosen to solve these equations because of its capability, simplicity and user friendliness. This software uses a finite volume-based discretization method. The computations are converged when the normalised residues for continuity and momentum equations are less than 0.0001.

4. Results and Discussion

4.1. Validation of mathematical modelling and numerical method

A two-dimensional computational domain has been constructed. EasyCFD[16] was used for construction of the geometry and for the present computations. The computational methodology and present modelling were validated by using the following methods.

- Comparing the present computational results with available results.
- Carrying out grid independence study.
- By checking the mass flow rate at the inlet and exit.

A grid independence study was carried out in the computational domain to rule out the influence of the mesh size (number of nodes in the computational domain. Also known as the grid size) on the results. Pressure loss coefficient (K_p) was kept at as a parameter to evaluate the performance of various mesh sizes. The static pressure loss coefficient was calculated as follows.

K_p = Static pressure loss coefficient = $\frac{\text{Static pressure at inlet} - \text{Static pressure at outlet}}{0.5 * \text{Density} * U_{in} * U_{in}}$ (14)

Table 2 presents of the results on the static pressure loss coefficient for various grid sizes. From the Table 2, computations with grid sizes above 59273 nodes in the computational domain did not show any significant difference for the pressure loss coefficient. Hence it was concluded to use a mesh size of about 60000 nodes for all computations.

The experimental data reported in[25] is employed to compare the results of present computational study. Figure 2 presents the comparison of computed and experimental vertical component of mean velocity profile at a distance of 2 duct widths from the elbow in the vertical arm of the duct for the configuration with 90^0 sharp bend. d is the distance across the duct and it has been non-dimensionalised using the duct width(D). It can be seen from the Fig. 2 that the computed and experimental mean velocity profiles at this location agree reasonably well.

TABLE 2. Effect of Grid Size on the Static Pressure Loss Coefficient (K_p)

The agreement is not 100% for the following two major reasons. (a). the computational domain considered in the current study is a two-dimensional domain whereas the experimental work was carried out in a three-dimensional setup and (b). at the inlet, uniform velocity condition has been imposed instead of a fully developed velocity profile that is more realistic. The validation of present methodology was carried out by monitoring the residuals during the computations and keeping balance of mass flow rate at the inlet and outlet. The mass flow rate difference between the inlet and the outlet is 0.001% which is very small.

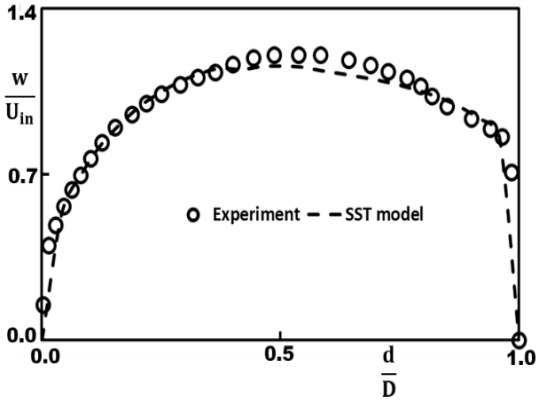

Fig. 2: Mean Vertical velocity profile comparison at the section 2D distance from the bend[25].

From the above validation studies, we are confident about our modelling strategy and hence the study was extended to other two-dimensional square duct configurations given Table 1. The computational results of simulations carried out for all geometries are presented in this section. Discussion on the prediction of static pressure loss coefficient are presented with results obtained using the Shear Stress Transport (SST) turbulence model, for various duct configurations.

4.2. Effect of Reynolds number on the static pressure loss coefficient (Kp)

In this section the results for the impact of flow Reynolds number on the static pressure loss coefficient are presented. Reynolds number of the flow was calculated using the inlet velocity and the duct width. The inlet fluid velocity was varied between 10 m/s to 60 m/s so that the Reynolds number varied from about 97000 to about 600000. Flow can be considered to be in the high Reynolds

Grid Size	Static Pressure Loss Coefficient (Kp)	Difference in Static Pressure Loss Coefficient (Kp)
46212	1.883	
47909	1.686	10.5 %
50510	1.547	8.2 %
55123	1.505	2.7%
59273	1.470	2.1%
64726	1.467	0.2%

number region for all geometrical configurations studied here.

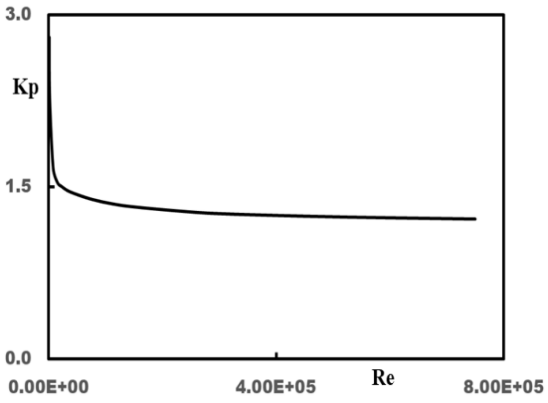

Fig. 3 Static pressure loss coefficient(Kp) with Reynolds number for a square duct with bend angle θ°=90.

Figure 3 presents the results for the effect of inlet velocity on the static pressure loss coefficient in the flow inside the duct with 90° sharp bend angle. Since similar trend was observed for other ducts with different bend angles, only results for the duct with 90° sharp bend angle are presented here. From the results presented in the Fig. 3, it is seen that the computed static pressure loss coefficient (Kp) varies very slightly as the Reynolds number goes up and that the static pressure loss coefficient tends to a constant value as is to be expected in high Reynolds number duct flow [20,26]. This constant value for the static pressure loss coefficient (Kp) for this flow inside the duct with 90° sharp bend is 1.467, this value of Kp matches closely to the value of 1.443 given for a square duct with a 90^0 sharp bend reported in [20].

4.3. Contours of magnitude of mean velocity inside the duct

In this section the contour plots of the magnitude of mean velocity for the flow inside ducts with various duct configurations are presented. All contour plots were generated using the same scale (colour scheme) for magnitude of mean velocity variation for all configurations. Figure 4 presents contour plots of magnitude of mean velocity inside the square ducts of various geometrical configurations.

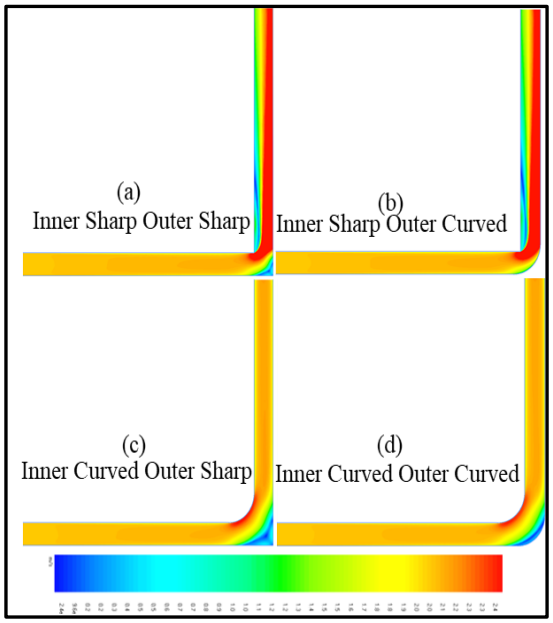

Fig.4. Contours plots of mean velocity magnitude inside various configurations

From the Figs. 4(a) and 4(b), it is seen that as the fluid approaches the sharp bend the magnitude of mean velocity distribution across the duct is changed and the high velocity fluid is seen moving towards the inner wall as if the fluid flow had anticipated the sharp bend. Further, after turning round the bend, the high velocity flow deviated towards the outer surface of the duct. At the bend, the fluid flow separated on the inner surface of the duct. Recirculation bubble can be seen, in the Figs. 4(a) and 4(b), clearly just after the bend. This low velocity region narrows the passage area through which the fluid can flow at the bend resulting in the increased velocity as the fluid flows past the bend. The flow reattached to the inner wall after some distance after the bend and further downstream fully-developed flow is re-established. The size of this separation bubble is reduced very much as the inner corner becomes smoothly curved. Also seen in the Figs. 4(a) and 4(b), is the low velocity region in the outer corner of the sharp bend. The size of this low velocity region is decreased in the configurations 4(c) and 4(d), as the inner corner becomes curved [Figs. 4(c) and 4(d)].

4.4. Contours of turbulent kinetic energy inside the duct

In this section the contour plots of the turbulent kinetic energy distribution for the flow inside ducts with various duct configurations are presented. All

contour plots were generated using the same scale (colour scheme) for turbulent kinetic energy variation for all configurations. Figures 5(a) and 5(b), show higher levels of turbulence in the entire domain with highest turbulent kinetic energy level at the bend where the fluid flow has just separated from the inner surface. In this recirculation region, the higher velocity flow went past by the separation region in which the fluid was moving in the opposite direction. As it can be seen from these figures that intensity of turbulence increases, both in size and magnitude, when the inner corner is sharp. The flow reattached to the inner wall after some distance after the bend and further downstream fully-developed flow is re-established. It is from the Figs. 5(c) and 5(d) that the size of the high region of turbulence is reduced very much as the inner corner becomes smoothly curved.

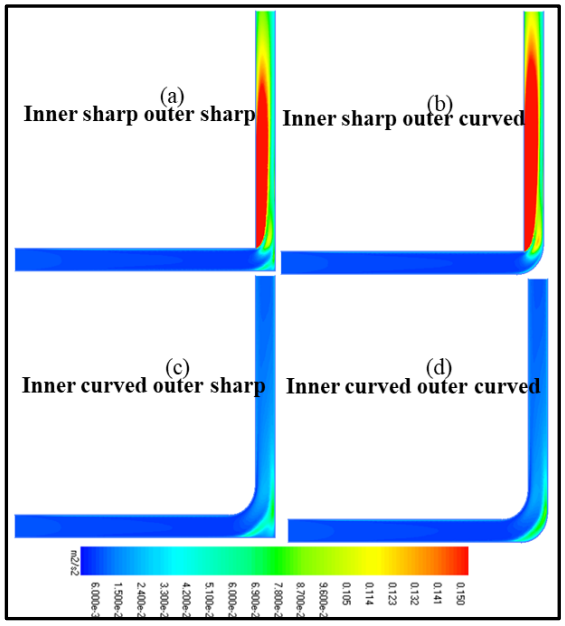

Fig.5. Contours of turbulent kinetic energy inside various configurations

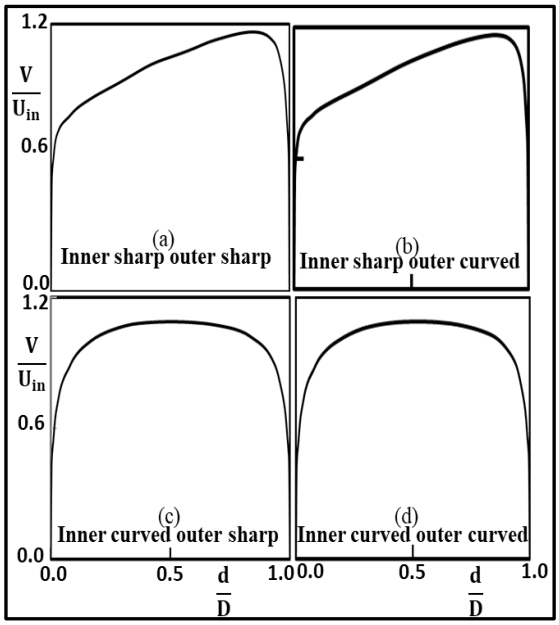

Fig.6. Magnitude of mean velocity profile at the outlet plane for various configurations

4.5. Magnitude of mean velocity profile at the outlet of the duct

Figure 6 presents the magnitude of mean velocity profiles at the outlet for the square ducts with various geometrical configurations. The magnitude of mean velocity has been non-dimensionalised by the maximum magnitude of mean velocity at the outlet(u_{max}) and the distance across the duct(d) is normalised by the width of the duct(D). From the Figs.6(a) and 6(b), it can be seen that the magnitude of velocity profile at the outlet is very asymmetric about the centreline of the duct agreeing with the results in the published literature [19,20]. It seen from the Figs. 6(c) and 6(d) that the asymmetry in the magnitude of mean velocity profile at the exit plane is reduced and the velocity profiles become symmetric when both corners are curved.

4.6. Wall shear stress variations on the inner and outer walls of the duct

In this section, the wall shear stress distributions on the inner and outer surfaces for all the duct configurations are presented. Figure 7 presents the variation of the wall shear stress distribution on the inner and outer walls from the inlet to outlet for the ducts.

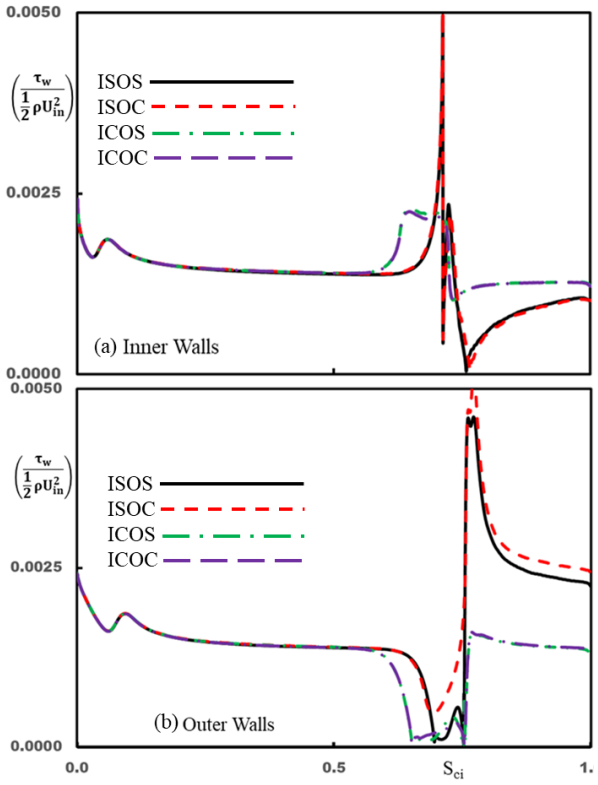

Fig. 7. Wall shear stress profiles on the duct walls

The wall shear stress has been non-dimensionalised by $(\frac{1}{2}\rho U_{in}^2)$ and the distance from the inlet to outlet along the inner and outer walls was converted into linear distance and non-dimensionalised using the maximum distance. This distance is S_{ci}. From the Fig. 7, it is seen that for the configurations for which the inner corner is sharp (ISOS and ISOC), the wall shear stress profiles on both walls start increasing and reaches a maximum value. This increase in the wall shear stress values on the walls start happening before the bend when the high velocity fluid is pushed towards the inner wall as seen in the contours of magnitude of mean velocity earlier. After reaching the maximum values, wall shear stress profiles start decreasing to reach the values almost close to the values at the start near the inlet. The affected region of the flow lies on the upstream and downstream of the bend. On the other hand, for the configurations for which the inner corner is curved (ICOS and ICOC), the wall shear stress variations along the walls of the duct do not show any dramatic increase or decrease in values and the increase is only very small inside the bend. From the Fig. 7 it is seen that the wall shear stress profiles along the walls of the duct recover quickly for the configurations (ICOS and ICOC) and values do not show much difference for these two configurations.

4.7 Magnitude of mean velocity along the middle line of the duct

Figure 8 presents the magnitude of mean velocity along the centreline in the computational domain for the ducts of various configurations.

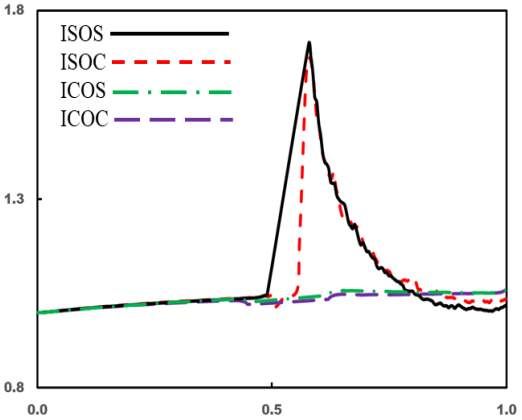

Fig. 8 Variation of the magnitude mean velocity along the middle line of the square duct

From the Fig. 8, it is seen that for the configurations for which the inner corner is sharp (ISOS and ISOC), the magnitude of mean velocity along the centreline starts increasing and reaches a maximum value. This increase in the magnitude of mean velocity along the centreline starts happening before the bend when the high velocity fluid is pushed towards the inner wall as seen in the contours of magnitude of mean velocity earlier. After reaching the maximum value, it starts decreasing to reach the values almost close to the values at the start near the inlet. The affected region of the flow lies on the upstream and downstream of the bend. On the other hand, for the configurations for which the inner corner is curved (ICOS and ICOC), the magnitude of mean velocity variations along the centreline of the duct do not show any dramatic increase or decrease in values and the increase is only very small inside the bend. From the Fig. 8 it is seen that the mean velocity along the centreline of the duct recovers quickly for the configurations (ICOS and ICOC) and values do not show much difference for these two configurations.

4.8 Variation of turbulent kinetic energy along the middle line of the duct

Configurations	(Maximum mean velocity at the exit)/Uin
ISOS	1.3489
ISOC	1.3441
ICOS	1.0725
ICOC	1.0621

Figure 9 presents the variation of turbulent kinetic energy along the centreline in the computational

Configurations	Maximum mean velocity location at the exit
ISOS	0.8682
ISOC	0.8495
ICOS	0.5212
ICOC	0.5005

domain for the ducts of various configurations.

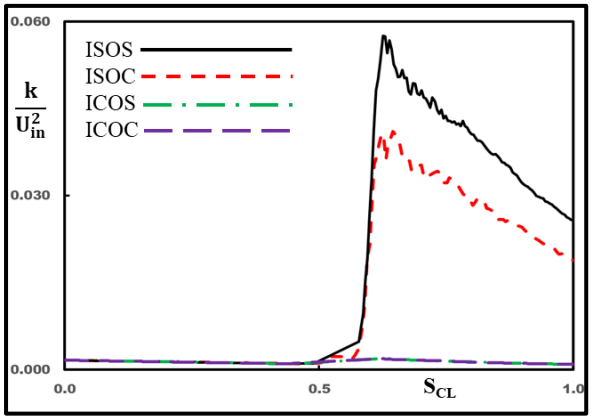

Fig. 9 Variation of turbulent kinetic energy along the middle line of the square duct.

From the Fig. 9, it is seen that for the configurations for which the inner corner is sharp (ISOS and ISOC), the turbulent kinetic energy along the centreline starts increasing and reaches a maximum value. This increase in the turbulent kinetic energy along the centreline starts happening before the bend when the high velocity fluid is pushed towards the inner wall, resulting in higher production turbulence, as seen in the contours of turbulent kinetic energy earlier. After reaching the maximum value, it starts decreasing. The affected region of the flow lies on the upstream and downstream of the bend. On the other hand, for the configurations for which the inner corner is curved (ICOS and ICOC), the turbulent kinetic energy variations along the centreline of the duct do not show any dramatic increase or decrease in values and the increase is only very small inside the bend. From the Fig. 9, it is seen that the turbulent kinetic energy along the centreline of the duct recovers quickly for the configurations (ICOS and ICOC) and values do not show much difference for these two configurations.

TABLE 3. Maximum mean vertical velocity values at the exit plane.

Table 3 shows the maximum values of magnitude of mean velocity at the exit plane. From this table, one can see that maximum mean velocity is the highest for the configuration ISOS and the configuration ICOC has the least value of maximum mean velocity at the exit plane.

TABLE 4. Location of maximum mean vertical velocity at the exit plane.

Also, it is seen that maximum values of mean velocity do not differ too much for the configurations ISOS and ISOC and similarly maximum values of mean velocity do not differ too much for the configurations ICOS and ICOC. The configurations ISOS and ISOC experience a large separate flow region in the sharp corners narrowing the fluid flow passage and, consequently, increasing the mean velocity in the narrow passage to maintain the mass flow rate. Fluid flow inside the configurations ICOS and ICOC do not experience large, separated flow regions at the turn allowing a wider passage for the fluid to flow resulting in lower velocity after the turn compared to the configurations ISOS and ISOC. It should be noted from the Table 3 that configurations ICOS and ICOC have lost the excess mean velocity which was imparted to the fluid flow at the bend showing that most of the static pressure loss has been recovered and it is seen that most of the static pressure loss can be recovered by modifying the inner sharp corner to a curved bend. Asymmetry in the mean velocity profile at the exit plane can be seen in the results presented in the Table 4. Table 4 presents the location of the maximum values of the magnitude of the mean velocity at the exit plane. The location of the maximum value of the mean velocity is estimated from the inner wall and non-dimensionalised using the duct width(D). The asymmetry imposed by the sharp bend on the mean

velocity is reduced when the corners are given a curvature. It is seen that most of the recovery to symmetry at the exit plane has been achieved by making the inner sharp corner alone curved. Table 4 shows, also, that the flow at the exit plane has become nearly symmetric when both corners were curved.

The peak values of the magnitude of mean velocity inside the computational domain for the flow inside ducts of various configurations are presented in the Table 5. From the Table 5 it is seen that that the maximum value of magnitude of velocity is high for the configuration ISOS. This increase in the peak of the mean velocity inside the computational domain is likely to be due to the narrowing down of the fluid passage because of the presence of recirculation regions both on the inner wall and the outer corner of the sharp bend. These circulation regions decrease in size with for the configurations ICOS and ICOC and consequently the peak values of the magnitude of mean velocity inside the computational domain are reduced. Also, it should be seen from the Table 5 that the configuration ICOC has the least peak value of magnitude of mean velocity in the computational domain closely followed by the configuration ICOS indicating that most of the disturbances caused by the sharp bend is reduced by giving a curvature to the inner corner alone.

Configurations	**(Maximum mean velocity in the domain) /Uin**
ISOS	2.0915
ISOC	1.9883
ICOS	1.2122
ICOC	1.1955

The peak values of the turbulent kinetic energy inside the computational domain for the flow inside ducts of various configurations are presented in the Table 6. The largest value of the turbulent kinetic energy (k_{max}) in the computational domain is non-dimensionalised using the velocity at the inlet (U_{in}^2). From the Table 6 it is seen that that the maximum value of turbulent kinetic energy is high for the configuration ISOS. This increase in the peak value of turbulent kinetic energy inside the computational domain is probably to be due to the production of turbulence at the sharp bends. These circulation regions decrease in size with for the configurations ICOS and ICOC and consequently the peak values turbulent kinetic energy inside the computational domain are reduced. Also, it should be seen from the Table 6 that the configuration ICOC has the least peak value of turbulent kinetic energy in the computational domain closely followed by the configuration ICOS indicating that most of the disturbances caused by the sharp bend is reduced by giving a curvature to the inner corner alone.

Table 7 presents the variation of reattachment length (SL) on the inner vertical wall of the duct for various configurations. The reattachment length (SL) on the inner wall is calculated from the inlet in the computational domain and is nondimensionalised by the total length of inner wall of the duct. From the Table 7, it is seen that the reattachment length on the inner wall for the square ducts with sharp corner (ISOS and ISOC) is large compared to the ducts with curved inner corners (ICOS and ICOC). This is due to the large size of the reattachment length on the inner wall of the square duct with sharp inner corners agreeing with the analysis established on the contours of mean velocity and the contours of the turbulent kinetic energy. Table 7, together with contours of magnitude of velocity and turbulent kinetic energy, shows that the recirculation becomes stronger in intensity (increase in turbulence) as well as recirculation length even if one of the corners is sharp. From the Table 7 it can also be seen that, the reattachment point moves close to the bend as the corners become smooth.

TABLE 5. Maximum magnitude of mean velocity in the computational domain.

Table 8 presents the variation of non-uniformity in the mean vertical velocity at the outlet plane of the duct. Non-uniformity is calculated using the Eqn. (15). From the Table 8, it is seen that the non-uniformity for the square ducts with sharp corner (ISOS and ISOC) is large compared to the ducts with curved inner corners (ICOS and ICOC).

TABLE 6. Maximum Turbulent Kinetic Energy in the computational domain.

Configurations	Non-uniformity in the mean velocity at the exit
ISOS	25.1 %
ISOC	23.2 %
ICOS	11.4 %
ICOC	04.8 %

Configurations	(Maximum Turbulent Kinetic Energy in the domain)/(Uin*Uin)
ISOS	0.165
ISOC	0.117
ICOS	0.021
ICOC	0.013

$$\beta = \frac{\sqrt{\frac{\Sigma(v_i - \overline{v})^2}{n-1}}}{\overline{v}} \quad (15)$$

where

β = Non-uniformity of velocity in the exit plane
v_i= Velocity at any point in the exit plane
$\overline{v}$ = average velocity in the exit plane
n = number of data points in the exit plane

TABLE 7. Reattachment point on the inner vertical wall.

Configurations	Reattachment point on the inner vertical wall
ISOS	0.8964
ISOC	0.8383
ICOS	0.6957
ICOC	0.6531

This is due to the reason that sharp corners produce more turbulence in the flow after the bend than the smooth corners as can be seen from the results of turbulent kinetic energy (Fig. 5 and Table 6). The reductions in the asymmetry and in the non-uniformity of the flow at the exit plane will be very useful in fluid processes and applications further downstream.

TABLE 8. Non-uniformity in the mean vertical velocity at the exit plane.

Table 9 presents the variation of static pressure loss coefficient (Kp) inside various duct configurations studied here. The static pressure loss coefficient (Kp) is calculated using the Eqn. (14). From the Table 9, it is seen that the static pressure loss coefficient (Kp) for the square ducts with sharp corner (ISOS and ISOC) is large compared to the ducts with curved inner corners (ICOS and ICOC).

TABLE 9. Static pressure loss coefficient in the duct.

Configurations	Static Pressure Loss Coefficient (Kp)
ISOS	1.467
ISOC	1.389
ICOS	0.263
ICOC	0.212

Conclusions

In this research work, the static pressure loss coefficient of several configurations of a square duct having 90^0 bends with and without corner modifications, in a two-dimensional turbulent fluid flow was studied. Inner sharp corner and outer sharp corner were altered separately and together to study the effects of corner modifications on the static pressure loss coefficient. Corner radius was fixed at Rc/D=1.33. There is a pressure loss in the square duct with sharp 90^0 bends. This is due to the large separation zones on the vertical wall and the sharp corner. It is shown that by changing the corners from sharp to smooth curvature static pressure loss coefficient can be reduced. The greatest reduction in static pressure loss coefficient occurs for the configurations when both corners were rounded (Configuration ICOC), causing a 85% decrease in the static pressure loss coefficient compared to a square duct with 90^o sharp bend (ISOS). It is shown that

major portion of static pressure loss reduction comes by giving a smooth curvature to the inner corner.

The flow patterns inside various geometries were significantly different, as revealed by the examination of the mean velocity and turbulence kinetic energy contours. The mean velocity on the centreline of the duct increases before decreasing. Mean velocity on the centreline of the duct is the highest for the configuration with both corners sharp (ISOS and ISOC). The values of turbulent kinetic energy on the centreline of the duct increases initially because of the turbulence generated by the sharp corners and then starts decreasing with streamwise distance for all cases. The sharp-cornered square duct produced the most turbulence kinetic energy. However, turbulent kinetic energy on the centreline of the duct is the lowest for the configurations with at least one round corner (ICOC and ICOS). The reattachment length on the inner vertical wall of the duct is the smallest for the square duct with both rounded corners (ICOC), followed by the square duct with inner corner rounded (ICOS). The square duct with sharp corners (ISOC and ISOS) had the highest reattachment length. The current computational study reveals that a large part of the static pressure loss recovery could be achieved by rounding the inner corner alone. The current study further reveals that the modification of outer corner alone does not help in reducing the static pressure loss in the square duct.

In conclusion, the round cornered square ducts may be more effective, and the corner shape of the square duct can have a considerable impact on the static pressure loss coefficient and fluid flow patterns. The present computational study shows that rounding off both sharp corners of a square duct with 90^0 bend results in reducing the static pressure loss, in the asymmetry of the mean velocity profile and non-uniformity at the exit plane, in the size of the separation zone on the inner vertical wall. These results could help in the design of more effective fluid flow systems such as ducts, pipelines and channels and have considerable implications for fluid mechanics and engineering.

References

[1] Weske JR, (1948). Experimental Investigation of Velocity Distributions Downstream of Single Duct Bends. NACA TN-1471, USA.

[2] Hellstrom LHO, Sinha A, Smits AJ., (2011). Visualizing the very-large-scale motions in turbulent pipe flow. Physics of Fluids 23:011703.

[3] Yamano H, Tanaka M, Ono A, Murakami T, Iwamoto Y, Yuki K, Sago H, Hayakawa S., (2009), Unsteady elbow pipe flow to develop a flow-induced vibration evaluation methodology. Int. Conf. on Fast Reactors and Related Fuel Cycles, Kyoto, Japan, 291-292.

[4] Sudo, K., Sumida, M., Hibara, H., (1998), "Experimental investigation on turbulent flow in a circular-sectioned 90-degree bend", Experiments in Fluids, Vol 25, pp. 42-49.

[5] Al-Rafai W.N., Tridimas, Y. D. and Woolley, N.H., (1990), "A study of turbulent flows in pipe bends ", Journal of Mechanical Engineering Science, Vol 204, pp. 399-408.

[6] Homicz, G.F., (2004), "Computational Fluid Dynamic Simulations of Pipe Elbow Flow", SAND Report, SAND 2004-3467, USA.

[7] Tanaka, M., Ohshima, H. And Monji, H., (2009), "Numerical investigation of flow structure in pipe elbow with large eddy simulation approach", Proceedings of the ASME 2009 Pressure Vessels and Piping Division Conference PVP2009, July 26-30, Prague, Czech Republic, PVP-77598.

[8] Humphery, J.A.C., Whitelaw, J.H. and Yee, G., (1981), "Turbulent flow in a square duct of strong curvature", Journal Fluid Mechanics, Vol 103, pp. 443–463.

[9] Taylor, A.M.K.P., Whitelaw, J.H. and Yianneskis, M., (1982), "Curved ducts with strong secondary motion: velocity measurements of developing laminar and turbulent flow", Journal Fluids Engineering, Vol 104, pp. 350–359.

[10] YILMAZ, A. and LEVY, E. K., (2001), "Formation and dispersion of ropes in pneumatic conveying", Powder Technology, Vol 114, pp. 165–185.

[11] Berger, S.A., Talbot, L. and Yao, L.S., (1983), "Flow in curved pipes," Annual Review of Fluid Mechanics, vol 15, pp. 461–512.

[12] Mumma, S.A., Mahank, T.A., and Yu-Pei Ke, (1998), "Analytical determination of duct fitting loss-coefficients", *Applied Energy*, Vol 61, pp. 229-247.

[13] Acheson, D.J., (1990), "Elementary Fluid Dynamics", Oxford Applied Mathematics and Computing Science Series, *Oxford University Press.* ISBN 978-0-19-859679-0.

[14] Batchelor, G. K., (1967), "An Introduction to Fluid Dynamics", Cambridge University Press, ISBN 978-0-521-66396-0.

[15] White, F. M., (2006), "Viscous Fluid Flow", McGraw-Hill, ISBN 978-0-07-124493-0.

[16] EasyCFD: A Two-dimensional Computational Fluid Dynamics software Manual Version 4.4.4, www.easycfd.net, 2020.

[17] Boikaego, T. and Subaschandar, N., (2023),"Heat transfer enhancement in solar water heater", AIP Conference Proceedings, Vol 2581, Issue 1, 090004, https://doi.org/ 10.1063 /5. 0126554

[18] Subaschandar, N.,2022," Prediction of Turbulent Flow past a Rectangular Cylinder", Journal of Xi'an University of Architecture & Technology (JXAT), China, Vol XIV, Issue 1, pp 142-158. ISSN: 1006-7930.

[19] Langwane, K. and Subaschandar, N., 2021, "Numerical Prediction and Reduction of Pressure Loss of Air Flow Inside a Sharp 90 Elbow Using Turning Vanes," WSEAS Transactions on Fluid Mechanics, Vol 16, pp 127-140. ISSN: 2224347X, 17905087**.**

[20] Gadiile, M. and Subaschandar, N., 2021," Pressure loss coefficients inside two-dimensional ducts with sharp bends", Journal of Xi'an University of Architecture & Technology, China. Vol XIII, Issue 9, pp. 142-158. ISSN: 1006-7930.

[21] Menter, F.R.,1993, "Performance of popular turbulence Models for attached and separated adverse pressure gradient flows ", AIAA Journal, Vol 30, No 8, pp 2066–2072.

[22] Menter, F.R., Kuntz, M., and Langtry, R., "Ten Years of Industrial Experience with the SST Turbulence Model," Turbulence, Heat and Mass Transfer 4, Ed: K. Hanjalic, Y. Nagano, and M. Tummers, Begell House, Inc., pp. 625–632, 2003.

[23] Van Doormaal, J.P. and Raithby, G.D., (1984), "Enhancement of SIMPLE method for predicting incompressible fluid flows", Numerical Heat Transfer, Vol 7, pp. 147-63.

[24] Menter, F.R. et al.,2003, "The SST Turbulence Model with Improved Wall Treatment for Heat Transfer Predictions in Gas Turbines", Proceedings of the International Gas Turbine Congress 2003 Tokyo, November 2-7.

[25] Mossad, R., Yang, W. and Schwarz, M.P., 2009, "Numerical prediction of Air Flow In a sharp 90 degree Elbow", 7th International Conference on CFD in the Minerals and Process Industries, CSIRO, Melbourne, Australia, 9-11, Dec 2009.

[26] Vijayan, P.K., Nayak, A.K., Kumar, N., 2019, Chapter 3-Governing differential equations for natural circulation systems, Single-Phase, Two-Phase and Supercritical Natural Circulation Systems. Eds: P.K.Vijayan, A.K. Nayak, N. Kumar, Woodhead Publishing, pp. 69-118. ISBN: 9780081024867, https://doi.org/ 10.1016/B978-0-08-102486-7.00003-2) .

.